The Astrophysical Journal Letters, 998:L3 (14pp), 2026 February 10 https://doi.org/10.3847/2041-8213/ac3749


# SN 2024afav: A Superluminous Supernova with Multiple Light-curve Bumps and Spectroscopic Signatures of Circumstellar Interaction

Harsh Kumar[1,2], Peter K. Blanchard[1,2], Edo Berger[1,2], Wasundara Athukoralalage[1], Daichi Hiramatsu[1,2,3], Sebastian Gomez[4], Moira Andrews[5,6], K. Azalee Bostroem[7,8], Joseph R. Farah[5,6], D. Andrew Howell[5,6], and Curtis McCully[5]

[1] Center for Astrophysics | Harvard & Smithsonian, 60 Garden Street, Cambridge, MA 02138-1516, USA; harsh.kumar@cfa.harvard.edu
[2] The NSF AI Institute for Artificial Intelligence and Fundamental Interactions, USA
[3] Department of Astronomy, University of Florida, 211 Bryant Space Science Center, Gainesville, FL 32611-2055, USA
[4] Department of Astronomy, The University of Texas at Austin, 2515 Speedway, Stop C1400, Austin, TX 78712, USA
[5] Las Cumbres Observatory, 6740 Cortona Drive, Suite 102, Goleta, CA 93117-5575, USA
[6] Department of Physics, University of California, Santa Barbara, CA 93106-9530, USA
[7] Steward Observatory, University of Arizona, 933 North Cherry Avenue, Tucson, AZ 85721-0065, USA
[8] LSST-DA Catalyst Fellow

*Received 2025 December 4; revised 2026 January 7; accepted 2026 January 8; published 2026 February 2*

## Abstract

We present a comprehensive optical and near-infrared (NIR) spectroscopic study of SN 2024afav, a hydrogen-poor superluminous supernova (SLSN-I) that peaks at $-20.7$ mag and exhibits an unusual multibumped light curve. Our spectroscopic observations, spanning phases of $-14$ to $+160$ days, reveal several unusual features: (i) a narrow (1800 km s$^{-1}$) and blueshifted (11,000 km s$^{-1}$) absorption from H starting at $+20$ days; (ii) persistent optical and NIR He I lines at all available phases, showing double absorption structure in NIR spectra at $+23$ days, with a high-velocity component at a similar velocity to H; (iii) early appearance of nebular [O III] emission starting at $+50$ days; and (iv) a strong [O II] + [Ca II] 7300 Å emission complex starting at $+110$ days. These unusual features, and their onset at the time of the light-curve bumps, provide compelling evidence of circumstellar interaction between the SN ejecta and a nearby hydrogen-rich shell, as well as the presence of helium in both the outer layers of the progenitor star and the circumstellar medium. A comparison of SN 2024afav to other SLSNe-I showing bumpy light curves and similar spectral properties (PTF 10hgi, SN 2017egm, SN 2019hge) points to a rare subgroup of SLSNe-I in which circumstellar medium interaction provides an important modulation to the energy input.

*Unified Astronomy Thesaurus concepts:* Supernovae (1668); Core-collapse supernovae (304); Circumstellar shells (242); Optical observation (1169); High resolution spectroscopy (2096); Spectroscopy (1558); Transient sources (1851); Near infrared astronomy (1093); Helium-rich stars (715)

*Materials only available in the online version of record: data behind figures, machine-readable table*

## 1. Introduction

Hydrogen-poor superluminous events are one of the brightest stellar explosion events in the Universe, with an absolute magnitude $M \lesssim -21$ and total radiated energy exceeding $10^{50}$–$10^{-51}$ erg (L. Chomiuk et al. 2011; R. M. Quimby et al. 2011; A. Gal-Yam 2012; M. Nicholl et al. 2015; D. A. Howell 2017; C. Inserra et al. 2017; R. Lunnan et al. 2018a; M. Nicholl 2021; T. J. Moriya 2024). Typically discovered in low-metallicity dwarf galaxies (R. Lunnan et al. 2014; D. A. Perley et al. 2016; T.-W. Chen et al. 2017; B. Hsu et al. 2024), these events exhibit characteristic O II and C II absorption features in their early-time spectra, indicating high temperatures, and show no signs of hydrogen (H) lines (P. A. Mazzali et al. 2016; M. Nicholl et al. 2016; R. M. Quimby et al. 2018; C. R. Angus et al. 2019; A. Gal-Yam 2019a, 2019b; A. Aamer et al. 2025). Recent large-scale sample studies of these events by Z. H. Chen et al. (2023), S. Gomez et al. (2024), and A. Aamer et al. (2025a) have revealed a significant diversity in their light-curve behavior and spectral properties, challenging the existing progenitor models.

The powering mechanism of superluminous supernovae (SLSNe-I) has been debated over the last few years. Several models of the SLSN-I powering mechanism have been proposed, such as a highly spinning, magnetized neutron star (magnetar) spin-down model (D. Kasen & L. Bildsten 2010; S. E. Woosley 2010; R. Lunnan et al. 2014; B. D. Metzger et al. 2015; D. A. Perley et al. 2016; T.-W. Chen et al. 2017; M. Nicholl et al. 2017; G. Hosseinzadeh et al. 2022; S. Gomez et al. 2024), interaction between dense ejecta and the circumstellar medium (CSM; E. Sorokina et al. 2016; J. C. Wheeler et al. 2017; R. Lunnan et al. 2018b; L. Yan et al. 2020; A. Fiore et al. 2021), pulsational/pair-instability supernovae (A. Gal-Yam et al. 2009; A. Kozyreva & S. Blinnikov 2015; M. Pursiainen et al. 2022; W. Lin et al. 2023), or fallback accretion (J. Dexter & D. Kasen 2013; T. J. Moriya et al. 2018). Among these, magnetar models are potentially the only ones that can consistently explain the peak luminosities of SLSNe based on large-scale light-curve fits, as shown in several recent studies (M. Nicholl et al. 2017; B. Hsu et al. 2021; S. Gomez et al. 2024).

While the magnetar spin-down model provides a good fit for the majority of the events, some SLSNe-I exhibit bumpy light

curves that deviate significantly from the smooth spin-down curve of the magnetar model. For example, a well-studied SN 2017egm shows a chaotic light curve that has been explained via a complex CSM interaction model (W. Lin et al. 2023; J. Zhu et al. 2023). Similar to SN 2017egm, some other SLSNe-I favor CSM interaction models over magnetars (E. Sorokina et al. 2016; J. C. Wheeler et al. 2017; R. Lunnan et al. 2018b; L. Yan et al. 2020; A. Fiore et al. 2021).

At least 30%, if not more, of the SLSNe-I exhibit multiple bumps in their postpeak light curves, unexplained by the favorite magnetar model (G. Hosseinzadeh et al. 2022). A few such examples are well-studied events, such as PTF 12dam (A. Tolstov et al. 2017), iPTF 13ehe (L. Yan et al. 2015), SN 2015bn (M. Nicholl et al. 2018), 2017egm (J. Zhu et al. 2023), PTF 10hgi (L. Yan et al. 2020), SN 2019hge (L. Yan et al. 2020), and SN 2019unb (S. J. Prentice et al. 2021), among others. The origin of these bumps has been a long-standing mystery. For some of the events where bumps appear to be somewhat periodic, J.-P. Zhu et al. (2024), and B. Zhang et al. (2025) used a magnetar precession-based model to explain their origin. Bumps in SN 2017egm, SN 2017gci, and other similar events were explained through CSM interaction models (S. Bose et al. 2018; A. Fiore et al. 2021; J. Zhu et al. 2023). J. R. Farah et al. (2025) used a Lense-Thirring (LT) precession model to explain non-periodic bumps in some of these events. While these models attempt to explain the early-time light-curve bumpy behavior, the majority of these events lack sufficient light-curve coverage to test these models over a longer period, where well-followed events like SN 2015bn clearly show nonperiodic behavior (M. Nicholl et al. 2018), suggesting a need for detailed follow-up of such events and spectroscopic study to unveil the mystery of the origin of bumps in SLSNe-I.

A handful of these bumpy events have shown very unusual spectroscopic signatures that deviate from the SLSNe-I spectra template. PTF 10hgi and other SLSNe-I present in L. Yan et al. (2020) are illustrative examples of such a sample. These objects show signs of helium and, in some cases, hydrogen as well, in their spectra. L. Yan et al. (2020) associate the presence of He I with bumps, suggesting that CSM interaction can provide a natural mechanism to excite helium and produce bumps in the light curves of these events. Similarly, in SN 2017egm, the presence of helium and [O III] is associated with a helium-rich CSM interaction with ejecta that is mainly dominated by oxygen, producing both features (S. Bose et al. 2018; J. Zhu et al. 2023). These events suggest that there exists a subclass of events where CSM interaction plays a crucial role in shaping the light curve and spectral features. These events may have a different progenitor channel or chaotic mass-loss history than those of typical SLSNe-I. A deeper understanding of the correlation between light-curve bumps, the presence of helium, and other unusual spectral features in the spectra is crucial for understanding the progenitor and explosion physics of these events.

We present SN 2024afav, an $M$ $-20.7$ luminosity SLSN-I with multiple bumps in the light curve. In the first work of a two-part series, we present a precessing magnetar model that can explain the first few bumps (J. R. Farah et al. 2025). The study suggested that the presence of late-time bumps could be explained by possible interaction with the CSM. Here, we present a detailed spectroscopic study of SN 2024afav to investigate the presence of CSM interaction and its implications on the light curve. Our extensive spectroscopic campaign reveals that SN 2024afav exhibits rare features, including the presence of early [O III] lines, the detection of helium, the emergence of a narrow hydrogen absorption line, and the appearance of late-time [O II] lines. We provide a detailed discussion on light-curve morphology, temperature evolution, spectral evolution, and a possible breakthrough in the detection of CSM interaction in SLSNe-I. This study represents a significant step toward a more detailed and systematic analysis of a large-scale sample of SLSN-I spectra with bumpy light curves. This Letter is outlined as follows. In Section 2, we describe the photometric and bolometric light curve, spectroscopic observations of SN 2024afav in Section 2. We provide the light-curve morphology and photometric evolution in Section 3, followed by spectroscopic evolution in Section 4. In Section 5, we discuss the unusual features in 2024afav and compare it to objects with similar light curves and spectral properties, and we discuss the implications of these features. Finally, we summarize the key results and outline the future direction of this study in Section 6.

## 2. Observations and Data

### 2.1. Discovery

SN 2024afav was discovered by the Asteroid Terrestrial-impact Last Alert System (ATLAS; J. L. Tonry et al. 2018) survey on 2024 December 12.71 UT with an ATLAS-orange magnitude of 18.3 at R.A. $= 12^{\rm h}49^{\rm m}12\overset{\rm s}{.}5$, decl.$= -18°06'12\overset{''}{.}61$ (A. Kumar et al. 2024). S. de Wet et al. (2025) classified SN 2024afav as a hydrogen-poor SLSN at a tentative redshift of $z$ 0.09 using spectra obtained on 2025 January 24. We used our high-quality spectra to refine the redshift to $z = 0.0724 \propto 0.0001$ ($d_L$ 340 Mpc), which we employ throughout this Letter. The SN is located $0\overset{''}{.}5$ from the center of a faint galaxy detected in Legacy survey images, with magnitudes of $m_g$ 22.2, $m_r$ 21.7, $m_i$ 21.6, and $m_z$ 21.6. At the redshift of the galaxy, the corresponding absolute magnitudes are $M_g$ $-15.3$, $M_r$ $-15.8$, $M_i$ $-16.0$, and $M_z$ $-16.0$. Using the Sloan Digital Sky Survey luminosity function from A. D. Montero-Dorta & F. Prada (2009), we infer a host luminosity of $L_g$ $1.47 \times 10^8\, L_{g,\odot} \approx 0.011 L_g^*$, $L_r$ $1.50 \times 10^8\, L_{r,\odot} \approx 0.006 L_r^*$.

### 2.2. Optical/UV Photometric Observations

We obtained multiband photometric observations using the Las Cumbres Observatory (LCO) network (T. M. Brown et al. 2013) and the Fred Lawrence Whipple Observatory[9] 1.2 m telescope equipped with Keplercam.[10] The observations were performed in the $g$, $r$, $i$, $z$ filters. The LCO data were reduced using the `lcogtsnpipe` pipeline (S. Valenti et al. 2016), while the Keplercam data were reduced using a python-based photometric pipeline following standard reduction procedures. In addition to our follow-up observations, we obtained publicly available photometry from ATLAS.

[9] https://www.cfa.harvard.edu/facilities-technology/cfa-facilities/fred-lawrence-whipple-observatory-mt-hopkins-az

[10] https://pweb.cfa.harvard.edu/facilities-technology/telescopes-instruments/12-meter-48-inch-telescope

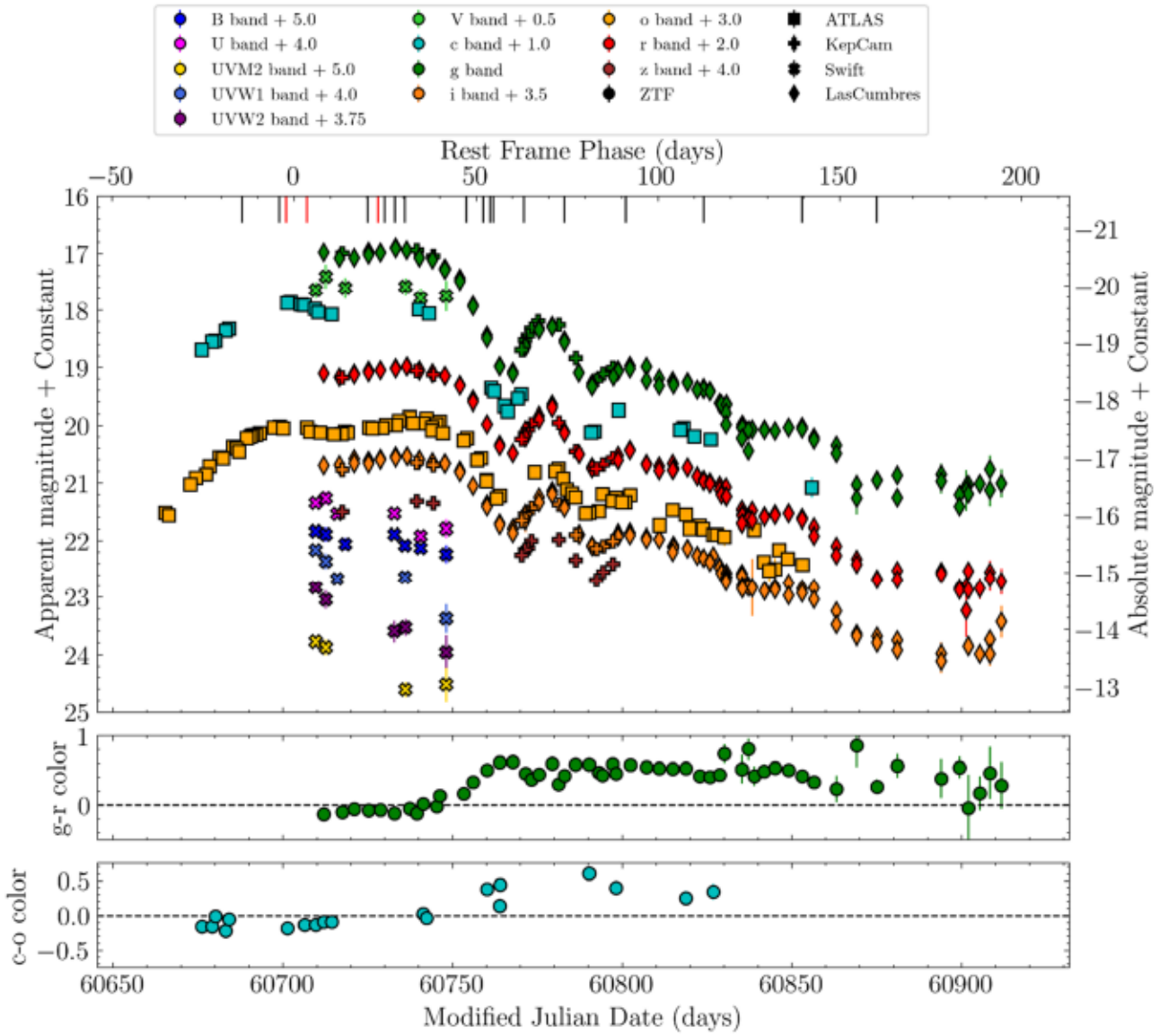


**Figure 1.** Optical/UV light curves of SN 2024afav with magnitudes in the AB system and corrected for Galactic extinction. The solid vertical ticks on the top axis mark the epochs of optical (black lines) and NIR (red lines) spectroscopic observations. The light curve rises from discovery to the first peak in 46 days and peaks at an absolute magnitude of $M_c$ −20.7. Subsequently, it exhibits a second peak of comparable brightness 38 days later before decaying sharply and displaying multiple subsequent undulations over the remainder of its evolution in all bands. The $g - r$ (green) and $c - o$ (blue) colors show an overall evolution from blue to red but with changes to bluer colors around the light-curve peaks.

We additionally obtained observations with the Neil Gehrels Swift UV/optical telescope in six filters, UVW2, UVM2, UVW1, *U*, *B*, and *V* (PI: Kumar), and utilized other publicly available UVOT data (PIs: Farah, Schulze). We performed photometry using `UVOTSOURCE`[11] of `HEASoft`, a part of the Swift software suite, with an aperture of 5 radius and standard aperture corrections.

The entire photometric campaign spans 255 days from the date of discovery (see Table 2 in the Appendix). A subset of the optical photometry has been previously presented in J. R. Farah et al. (2025). The photometric dataset presented here is in the AB magnitude system for all filters and has been corrected for Galactic extinction, with $E(B - V) = 0.062$ mag (E. F. Schlafly & D. P. Finkbeiner 2011), assuming the E. L. Fitzpatrick (1999) reddening law with $R_V = 3.1$. No host extinction correction has been applied. The multiband light curves are shown in Figure 1. The *c*, *o* band and pseudobolometric light curves peak at MJD = 60703.3, which we use as phase = 0 throughout this Letter (see Figure 2 and Section 3 for details).

### 2.3. Optical Spectroscopic Observations

Following the initial classification of SN 2024afav as an SLSN-I, we obtained an extensive spectroscopic sequence spanning phases of +20 to +160 days using LCO, the 6.5 m MMT, the 6.5 m Magellan telescopes, and the 8.2 m Gemini-South telescope. Additionally, we included publicly available spectra on WISeREP[12] (O. Yaron & A. Gal-Yam 2012) obtained at −14 and −4 day phases.

[11] https://www.swift.ac.uk/analysis/uvot/mag.php

[12] https://wiserep.org

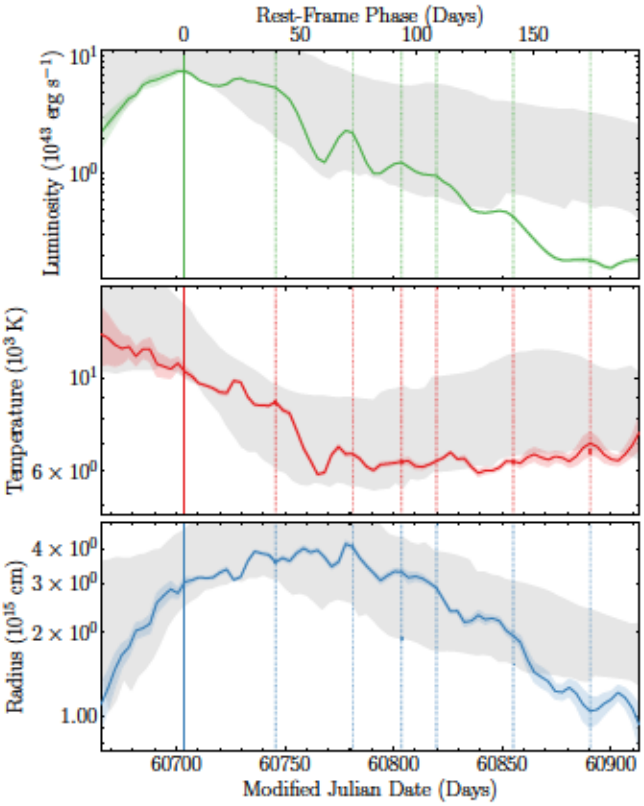


**Figure 2.** The pseudobolometric light curve (top), photospheric temperature (middle), and photospheric radius (bottom) of SN 2024afav. The gray shaded regions represent the range of parameters for quantities in the SLSN-I population, as reported by S. Gomez et al. (2024). The pseudobolometric light curve exhibits multiple bumps (marked by vertical lines). The peak luminosity and width of each peak are provided in Table 1. The temperature and radius fluctuations closely follow the peaks.

Low-resolution ($R$ 400) spectra were obtained with the FLOYDS spectrographs mounted on the 2 m LCO Faulkes telescopes North at Haleakalā and South at Siding Spring, Australia. The observations were undertaken as part of the Global Supernova Project from phase +20 to +91 days. We used a 2 slit along the parallactic angle (A. V. Filippenko 1982), covering a wavelength range of 3400–10,000 Å. One-dimensional spectra were extracted, reduced, and calibrated following standard procedures using `floyds_pipeline`[13] (S. Valenti et al. 2014).

On MMT, we used the Binospec spectrograph (D. Fabricant et al. 2019) with the LP3800 filter in combination with the 270 lines mm$^{-1}$ grating and a 1 wide slit covering a wavelength range of 3825–9200 Å with $R$ 1500. Two spectra were obtained at phases of +54 and +139 days.

We used the Low Dispersion Survey Spectrograph 3 (K. B. Stevenson et al. 2016) on the Magellan/Clay 6.5 m telescope with the VPH-All grism and a 1 wide slit, covering a wavelength range of 4265–9650 Å with $R$ 700. Four spectra were obtained at phases spanning +30 to +160 days. Furthermore, we obtained a high-resolution spectrum using the Magellan Inamori Kyocera Echelle (MIKE), with three exposures of 1800 s each at 2 × 2 binning and a 1 wide slit resulting in a resolution of $R$ 19,000 and $R$ 25,000 on the red and blue sides, respectively, covering a wavelength range of 3350–9500 Å at a phase of +53 days.

[13] https://github.com/LCOGT/floyds_pipeline

We used the GMOS spectrograph on the Gemini-South telescope to obtain a spectrum at a +24 day phase with the R150 grating, the GG455 filter, and a 1 wide slit, covering a wavelength range of 4744–9999 Å with $R$ 300.

The spectra from MMT, Magellan, and Gemini were reduced using the `PypeIt` package (J. X. Prochaska et al. 2020a) in a standard manner. The one-dimensional spectra were extracted and flux-calibrated using a standard star observation obtained with the same configuration. Data from the high-resolution MIKE spectrograph were reduced using a python-based `CarPy` pipeline (D. D. Kelson et al. 2000; D. D. Kelson 2003).

### 2.4. NIR Spectroscopic Observations

We obtained near-infrared (NIR) spectra with FLAMINGOS2 (S. Eikenberry et al. 2006) on Gemini-North and GNIRS (J. H. Elias et al. 2006) on Gemini-South. The FLAMINGOS2 spectra were obtained at phases of −2 and +3 days using the medium-resolution configuration with a 2 pixel wide slit and an HK filter, covering 1.26–2.50 $\mu$m with $R$ 900. The GNIRS spectrum was obtained at a phase of +23 days with the short camera, a 32 lines mm$^{-1}$ grating, and a 3 pixel wide slit and cross-dispersed, covering a wavelength range of 0.82–2.52 $\mu$m with $R$ 1200. The NIR spectra were reduced using the `Pypeit` package, including flat-fielding using GCALflats and sky subtraction obtained on the same night as the spectra. Flux calibration was performed on the extracted spectra using standard star observations obtained on the same night. Finally, a telluric correction was applied to account for atmospheric absorption features.

## 3. Light-curve Evolution

### 3.1. Light-curve Morphology

The multiband light curves of SN 2024afav, shown in Figure 1, exhibit an unusual evolution. The light curve rises for 46 days after discovery and peaks at MJD 60703.3 with $M_c$ −20.70 and $M_o$ −20.51 ($k$-corrected; D. W. Hogg et al. 2002). The light curve shows a slight dip in brightness following the initial peak, and then brightens again to a second, equally bright peak at +40 days, with $M_c$ −20.60, $M_o$ −20.57, and $M_g$ $M_r$ −20.50. Following the second peak, the light curve shows a sharp decline, followed by a third peak at +72 days with $M_g$ −19.3 and $M_r$ −19.9. After the first three peaks, the light curve shows four more low-scale undulations at +94 with $M_r$ −19.1, at +109 with $M_r$ −18.8, at +142 with $M_r$ −18.0, and at +175 with $M_r$ −17.0. The light curve starts to show the start of another peak; however, no photometric coverage is available due to visibility constraints. The peak absolute magnitude is at the 78th percentile of the SLSN-I population (S. Gomez et al. 2024).

The $g - r$ and $c - o$ colors are initially −0.2–0 mag during the first two peaks and then redden rapidly after the second peak to a mean value of +0.6 mag. However, the densely sampled $g - r$ color curve exhibits changes to a bluer color at the time of subsequent light-curve peaks.

### 3.2. Temperature and Radius Evolution

We used the `extrabol python` package (I. Thornton et al. 2024) to determine the bolometric light curve, photospheric

**Table 1**
The Properties of Significant Peaks in the Pseudobolometric Light Curve

| Peak Number | MJD | Phase (days) | $L_{bol}$ (erg s$^{-1}$) | FWHM (days) |
|---|---|---|---|---|
| 1 | 60703.3 | 0 | $7.48 \times 10^{43}$ | 23.0 |
| 2 | 60745.7 | +40 | $5.41 \times 10^{43}$ | 29.6 |
| 3 | 60781.1 | +72 | $2.24 \times 10^{43}$ | 8.8 |
| 4 | 60803.7 | +94 | $1.25 \times 10^{43}$ | 12.1 |
| 5 | 60819.8 | +109 | $0.96 \times 10^{43}$ | 11.6 |
| 6 | 60851.9 | +142 | $0.48 \times 10^{43}$ | 12.5 |
| 7 | 60890.5 | +175 | $0.18 \times 10^{43}$ | 14.1 |

temperature, and radius evolution of SN 2024afav, assuming a blackbody spectrum. The results are shown in Figure 2. We fit a smooth curve to the overall light curve using a large bin size of 30 to minimize the effects of undulation on the fitted curve. This trend was then subtracted from the bolometric light curve, and the `scipy.signal.find_peakspython` package was used to get the peaks in the light curve. Including the primary peak, the light curve shows a total of seven peaks in the bolometric light curve (see Table 1). We estimate a peak luminosity of $7.5\times10^{43}$ergs$^{-1}$ for the primary peak. The positions, peak bolometric luminosity ($L_{p,\,bol}$) and half widths, for all peaks in the light-curve have been listed in Table 1. Integrating the light curve, we find a total radiated energy of $5.1 \times 10^{50}$ erg, on the lower end of the SLSN-I population (S. Gomez et al. 2024).

The temperature declines from 12,700 K at the first epoch to 10,340 K until the primary peak. Thereafter, the temperature decreases further to 8500 K around the secondary peak before showing a sudden decline to 5900 K at the +60 day phase. After this epoch, the temperature shows a rise to 6870 K, following the third peak in the light curve at the +70 day phase. After the third peak, the temperature evolution shows small fluctuations, closely follows the light-curve undulations, and remains close to 6000 K.

The photospheric radius shows an increase from $10^{15}$ cm at first detection to $3 \times 10^{15}$ cm at the primary peak. Subsequently, the radius continues to rise more gradually past the secondary peak to a maximum value of $3.9 \times 10^{15}$ cm at +40 days. The radius then declines back to $10^{15}$ cm at +180 days. Throughout this overall evolution, the photospheric radius exhibits smaller fluctuations during the multiple light-curve peaks.

### 3.3. X-Ray Observations

We analyzed Swift X-Ray Telescope (XRT; 0.3–10 keV) observations obtained in conjunction with UVOT observations and did not detect any emission at the location of SN 2024afav. We estimate a $3\sigma$ upper limit using the Swift-XRT web tool[14] (P. A. Evans et al. 2007; P. A. Evans et al. 2009). Using a Milky Way H I density of $3.71 \times 10^{20}$ (R. Willingale et al. 2013) and assuming a power-law spectrum with a photon index of 2, we estimate an average source unabsorbed flux limit of $F_X \lesssim 5.7 \times 10^{-13}$ erg s$^{-1}$ cm$^{-2}$, corresponding to a luminosity limit of $L_X \lesssim 7.8 \times 10^{42}$ erg s$^{-1}$. This limit is not particularly constraining relative to typical SLSN-I X-ray detection luminosities of $\leqslant 10^{41}$ erg s$^{-1}$ (R. Margutti et al. 2018).

[14] https://www.swift.ac.uk/user_objects/index.php

## 4. Spectroscopic Analysis

### 4.1. Optical Spectral Evolution Overview

The complete optical spectral sequence from phase −14 to +160 days is shown in Figure 3, and a detailed identification of features using SN 2017egm, PTF 10hgi, and median spectra from A. Aamer et al. (2025) is marked in Figure 4 at the +51 and +112 day phases. The spectral evolution follows a typical trend observed in SLSNe-I, from a hot, blue continuum with absorption lines at early times to a cooler, emission-line-dominated spectrum in the near-nebular phase. The early prepeak spectra exhibit the typical "w"-shaped broad features of O II in the 3500–5000 Å region with a velocity of 11,600 km s$^{-1}$. The early spectra also show features in the 5000–6000 Å region commonly associated with Na I D and Si II and sometimes He I (Z. H. Chen et al. 2023; S. Gomez et al. 2024; A. Aamer et al. 2025a).

Postpeak, as the temperature declines to $\lesssim 10^4$ K, the O II lines weaken, and the 3500–5000 Å region is dominated by Fe II and Fe III lines with the noticeable presence of a 5169 Å feature. The 5000–6500 Å region shows three absorption features that increase in strength over time, which we identify as the He I 5876 Å and Na I D 5890, 5896 Å complex, O I 6150 Å, and Si II 6355 Å. In addition to the strong He I 5876 Å feature, we see the presence of other relatively weaker He I 6678, 7065, and 7281 Å features. Meanwhile, O I 7774 Å appears in the +20 day spectrum and becomes stronger over time until +63 days, where it starts to show an associated emission component. From +20 to +74 days, the velocity decreases from 7500 to 6300 km s$^{-1}$, estimated using isolated Si II and O I features.

Starting at a phase of +91 days, the spectra begin to exhibit near-nebular emission lines of Mg I] 4571 Å and the Ca II 8498, 8542, 8662 Å NIR triplet. Furthermore, the O I 7774 Å feature changes from absorption to emission and becomes stronger over time until our last spectrum at +160 days. We estimate a velocity of 6000 km s$^{-1}$ at a phase of 100 days using O I 6158 and 7774 Å. Moreover, we find an emission feature of [Ca II] and [O II] centered at 7300 Å starting at +112 days, which becomes stronger thereafter. This feature is discussed in detail in Section 4.2.

SN 2024afav spectral features exhibit lower velocities than the median spectra of SLSNe-I (A. Aamer et al. 2025), as shown in Figure 3. The spectral evolution, features, and velocity progression most closely resemble those of the unusual events SN 2017egm and PTF 10hgi (L. Yan et al. 2020; J. Zhu et al. 2023), which share a few distinctive features in their optical spectra. We discuss the distinctive feature in detail in Sections 4.2 and 5. The spectral similarities from the peak to postpeak phases make SN 2024afav a spectral analog of PTF 10hgi and SN 2017egm events.

### 4.2. Unusual Spectral Features

While most of the spectral features in SN 2024afav are typical of SLSNe-I, some are unusual; we show the evolution of these features in Figure 5 and discuss them in detail below.

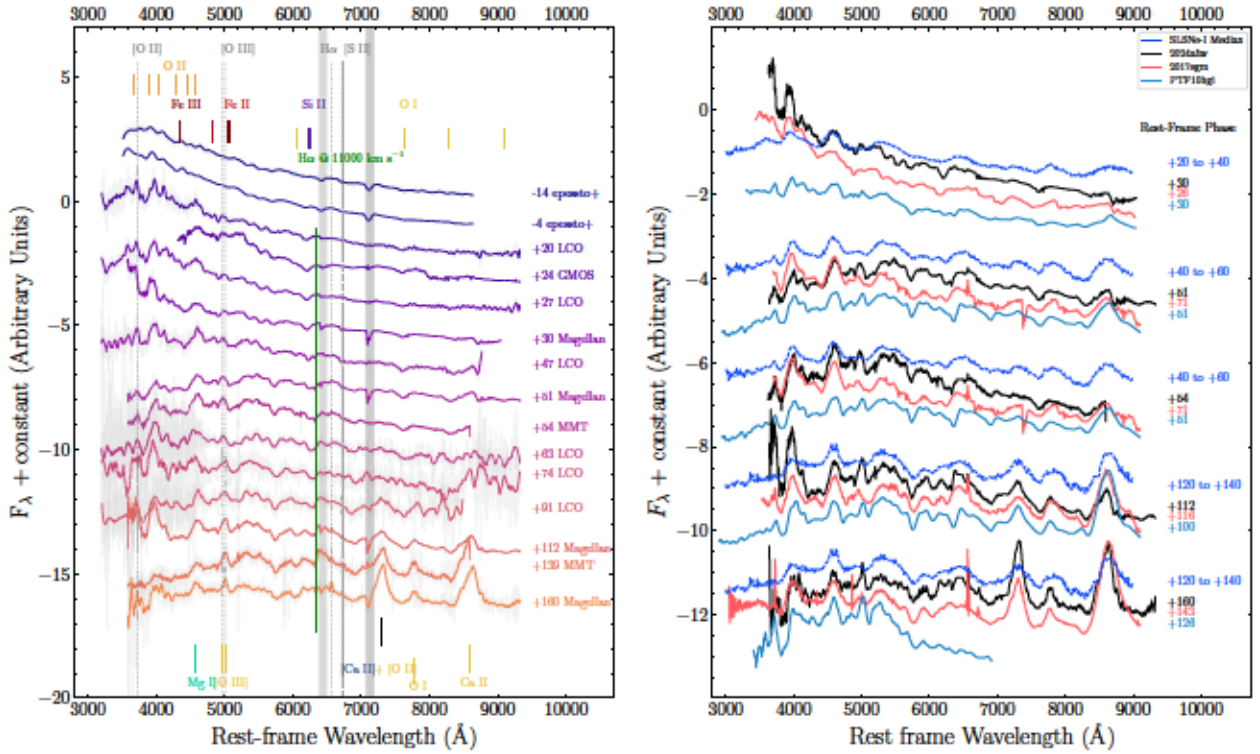


**Figure 3.** Left: optical spectra of SN 2024afav covering phases of −14 to +160 days. The early-time spectra are blue, with characteristic O II features. In the postpeak phases, we observe other common SLSN-I features of Fe II, Fe III, Na I D, Si II, and O I, along with unusual narrow features such as [O III] emission and H absorption. The $\gtrsim$+112 day spectra show a nebular NIR Ca II triplet and a [Ca II] + [O II] complex. The colored spectra are smoothed using the Savitzky–Golay filter (M. A. Selver et al. 2018). Right: comparison of SN 2024afav spectra to SN 2017egm, PTF 10hgi, and median SLSN-I spectra (A. Aamer et al. 2025) at several phases. SN 2024afav shows remarkable similarity to SN 2017egm, PTF 10hgi, and SN 2019hge, including the unusual [O III] and [Ca II] + [O II] complex emission features. The narrow H feature in the SN 2024afav spectra is at a similar velocity and width to H in PTF 10hgi (L. Yan et al. 2020). A detailed identification of all features in the postpeak phase is provided in Figure 4.

(The data used to create this figure are available in the online article.)

#### 4.2.1. [O III] 4969, 5007 Å

From +20 days onward, we observe an unusual emission feature at 4940 Å with a possible absorption component centered at 4880 Å. The overall profile of the emission feature changes with time, with the peak shifting to a wavelength of 5000 Å at later epochs (left panel of Figure 5). While it is plausible to associate this unusual absorption and emission feature with Fe II 4924 Å, a detailed study of the SLSN-I sample shows that Fe II 5169 Å is stronger than Fe II 4924 Å at all phases (A. Aamer et al. 2025), but we do not find a strong Fe II 5169 Å feature in SN 2024afav. This and the shift in the line centroid indicate that this feature is not predominantly due to Fe II 4924 Å and instead has a significant contribution from the [O III] 4969, 5007 Å doublet. Using our high-resolution MIKE spectrum at +53 days, we fit the emission profile and find the definitive presence of [O III] 4969, 5007 Å (FWHM 66 Å), as well as a contribution from Fe II 4924 Å (Figure 5). Based on the overall evolution from early to later phases, we conclude that at $\lesssim$+50 days, this feature is a complex of Fe II 4929 Å and [O III] 4959, 5007 Å. At $\gtrsim$+50 days, the [O III] feature becomes stronger, explaining the wavelength shift and enhanced strength of this emission feature compared to typical SLSNe-I.

#### 4.2.2. H

We observe a narrow absorption feature centered at 6330 Å starting at +30 days (and potentially even at +20 days; middle panel of Figure 5). We identify this feature as a potential high-velocity H absorption using a spectral match to PTF 10hgi (L. Yan et al. 2020). This feature retains a nearly constant velocity of −11,000 km s$^{-1}$ and a narrow FWHM width of 1800 km s$^{-1}$. Using our high-resolution MIKE spectrum at +53 days, we fit the profile of this feature and find that it requires an additional weak emission component on the bluer side (bottom right panel of Figure 5), which we identify as a potential O I 6300 Å feature. We conclude that the absorption feature is narrow, blueshifted H retaining constant velocity and width throughout the spectral sequence.

#### 4.2.3. [O II] 7319, 7330 Å and [Ca II] 7292, 7324 Å

A distinctive emission profile emerges at 7300 Å at +112 days (right panel of Figure 5). This feature shows some asymmetry on the bluer end due to the presence of He I 7281 Å. We fit a multi-Gaussian profile and find three components in the line profile: a narrow component centered at 7330 Å, a wider component at 7300 Å, and a broad, lower-intensity component fitting the continuum. We identify these features as the [O II] 7319, 7330 Å and [Ca II] 7292, 7324 Å doublets. The center of the overall profile is closer to the [O II] doublet, implying that the feature is dominated by [O II]. Additionally, this feature becomes stronger at the same time when the [O III] 5007 Å feature becomes weaker at $\gtrsim$+100 days, implying a transition from [O III] to [O II]. For our spectra at $\gtrsim$+112 days, we estimate the $L_{7300}/L_{6500}$ ratio 4.82 $\alpha$ 1.14 using the 7300 Å and

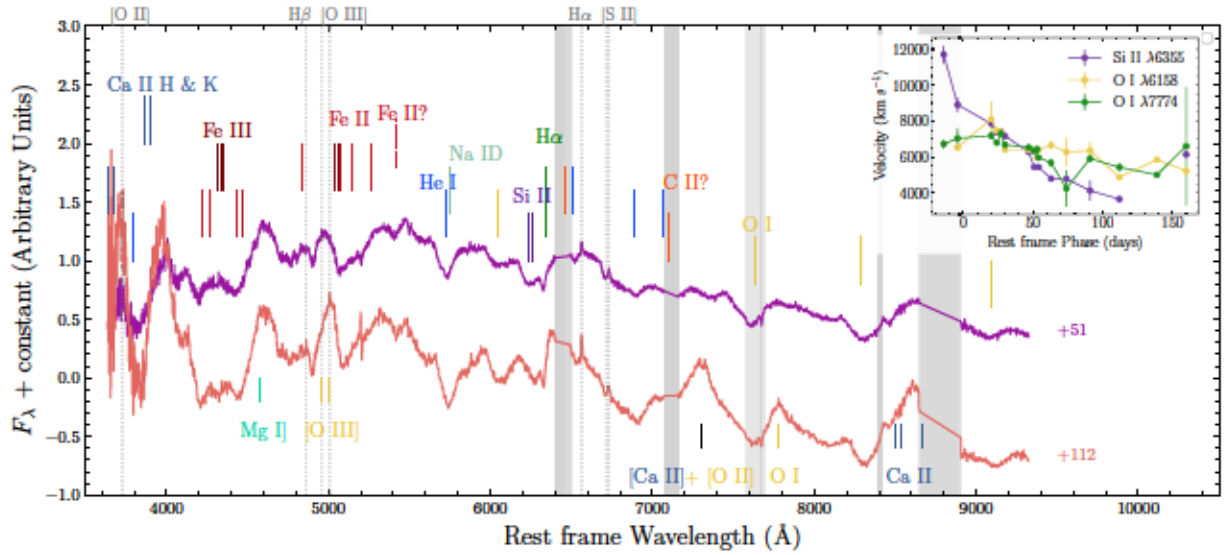


**Figure 4.** Detailed identification of spectral features in the optical spectra at +51 and +112 days. The majority of the absorption features are marked above the spectra using a blueshifted velocity of 7500 km s$^{-1}$, while the Fe II, Fe III, and Si II are at 5500 km s$^{-1}$. The SN emission features are marked below the spectra at their rest-frame wavelengths. The host galaxy emission lines are marked with vertical gray dotted lines. The inset shows the photospheric velocity evolution estimated using relatively isolated features of Si II 6355 Å, O I 6158 Å, and O I 7774 Å (also see Table 3).

6300 Å features. The $L_{7300}/L_{6300}$ ratio for SN 2024afav is greater than the typical values estimated from other SLSNe-I (M. Nicholl et al. 2019; P. K. Blanchard et al. 2025). Furthermore, the ratio estimated from the $\gtrsim$+100 day phase spectra of SN 2024afav exhibits an increasing trend (see Table 4 in the Appendix), similar to some SLSNe-I such as SN 2017egm, PTF 10hgi, and LSQ 14an that show possible CSM interaction (M. Nicholl et al. 2019; P. K. Blanchard et al. 2025).

### 4.3. NIR Spectroscopic Analysis

We show the NIR spectra of SN 2024afav in Figure 6. The near-peak NIR spectra obtained at −2 and +3 days cover 1.35–2.3 $\mu$m and exhibit a single broad absorption feature, corresponding to He I $\lambda$2.058 $\mu$m (hereafter the He I 2 $\mu$m line) with a blueshifted velocity of −10,500 km s$^{-1}$, similar to photospheric velocities from optical spectra at these phases. No other features are detected, for example, S I, Mg I, and Si I, which are commonly observed in Type Ib/c (M. Shahbandeh et al. 2022).

The next NIR spectrum at +23 days, covering 0.78–2.3 $\mu$m, exhibits the same He I 2 $\mu$m absorption but with an apparently bimodal velocity structure, with velocities of 7500 and 10,500 km s$^{-1}$ (inset of Figure 6). The strongest feature in the spectrum, at 1.05 $\mu$m, is a blend of Mg II $\lambda$1.095 $\mu$m, He I $\lambda$1.083 $\mu$m, and possibly C I $\lambda$1.069 $\mu$m (see Figure 6). This absorption feature also shows two distinctive absorption troughs at 1.045 and 1.055 $\mu$m, mirroring the profile of the He I 2 $\mu$m line. The possible blend of several features in this wavelength range makes the interpretation of the line profile complicated, but the similarity to the unblended He I 2 $\mu$m line suggests that it is dominated by He I $\lambda$1.083 $\mu$m at two different velocities. Additionally, it shows a series of absorption features centered at 8250, 9000, 9700 Å. These features correspond to O I 8446 Å, 9263 Å with a possible contribution from C I 8335 Å, 9405 Å and Mg II 9218, 9244 Å features; however, we do not see conclusive evidence of carbon lines in the optical spectra and no signs of Mg II 21062 Å features, suggesting that the NIR features are likely dominated by oxygen. Regardless of the interpretation, we conclusively detect He I, providing strong evidence of its presence in ejecta of SN 2024afav.

## 5. Discussion

### 5.1. Spectroscopic Evidence for Postpeak CSM Interaction

The presence of narrow and blueshifted H absorption and persistent He I optical and NIR lines and the early appearance of forbidden high-ionization oxygen line emission ([O II] and [O III]) are highly unusual for SLSNe-I. By definition, these events do not show signatures of hydrogen, with the exception of a few events that, unlike SN 2024afav, showed hydrogen only at a very late time (L. Yan et al. 2017). The He I features have similarly only been detected in a few SLSNe-I to date, generally near peak, when a small amount of helium retained by the progenitor is nonthermally excited by the central magnetar (P. A. Mazzali et al. 2016; M. Nicholl et al. 2019; S. Gomez et al. 2024). These features weaken in the postpeak phase when the ejecta expand and the engine energy input declines, as seen recently in SN 2024rmj (H. Kumar et al. 2025). The late-time presence of He I in SN 2024afav requires a different excitation mechanism, likely CSM interaction (e.g., L. Yan et al. 2020; L. Dessart 2024a). Similarly, when detected, the [O II] and [O III] lines are generally observed only in the late nebular phase, indicative of ionization of the inner ejecta by the central engine (M. Nicholl et al. 2019; P. K. Blanchard et al. 2025). In a few cases, the early appearance of [O III] has been interpreted as a signature of CSM interaction (A. Aamer et al. 2024; S. Schulze et al. 2024). We thus conclude that the appearance and properties of these features are indicative of CSM interaction in the postpeak phase.

The narrow width, large blueshift, and appearance starting at only +20 days of H absorption are distinct from other spectral features in SN 2024afav (Figure 4), suggesting that hydrogen is not part of the initial SN ejecta and was instead swept up by the fast ejecta from the surrounding CSM. The

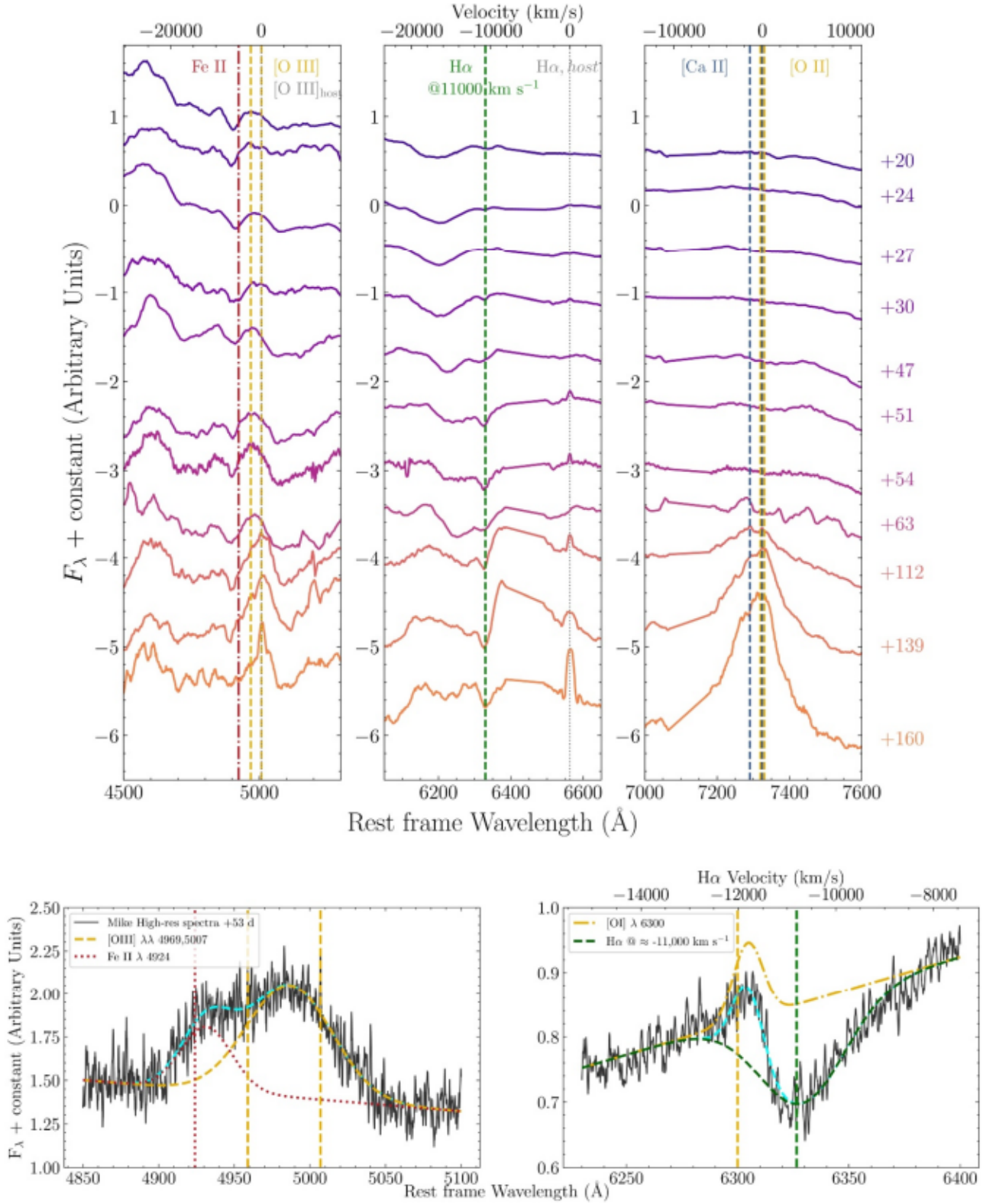


**Figure 5.** Top: evolution of the unusual spectral features [O III] (left), H (middle), and the [O II] + [Ca II] complex (right). The [O III] feature exhibits contamination from Fe II in early spectra and displays a shift toward [O III] over time. The H feature (green dashed line) is narrow (1800 km s$^{-1}$) and remains at a constant blueshift velocity of 11,000 km s$^{-1}$. The [O II] + [Ca II] complex appears at +112 days and becomes stronger over time. This feature is centered on [O II], implying the stronger presence of [O II] compared to [Ca II]. Telluric absorption is masked in the middle and right panels. Bottom: line fits to the [O III] 4969, 5007 Å (left) and H (right) profiles in the MIKE spectrum at +53 days. The fitted profile shows a clear presence of [O III] and a contribution from Fe II 4924 Å. The H profile exhibits asymmetric absorption, which is due to emission from [O I] 6300 Å.

lack of a H emission component further indicates that the hydrogen was most likely present in a narrow shell rather than in a diffuse CSM, commonly seen in interacting SNe such as SN IIn (L. Dessart et al. 2016; R. A. Chevalier & C. Fransson 2017; L. Dessart & D. J. Hillier 2022; L. Dessart 2024b).

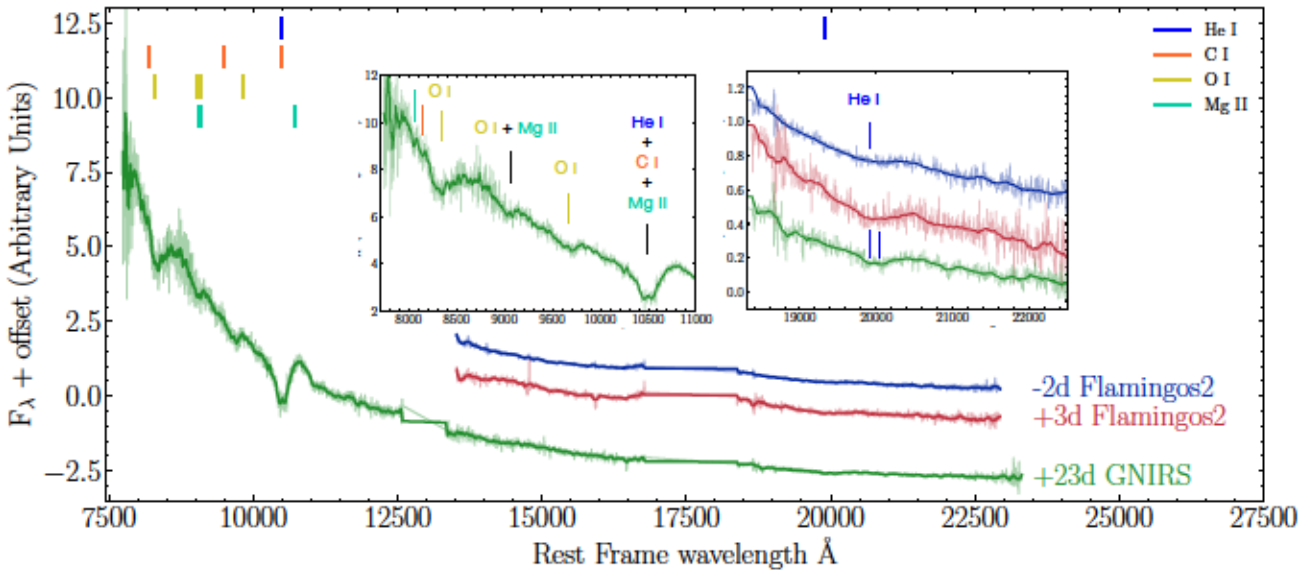


**Figure 6.** NIR spectra at −2, +3, and +23 days. The insets show zoomed-in versions of the spectra in the 1 and 2 μm regions. All three spectra show He I λ2.058 μm, implying the presence of helium in the ejecta. The 1 μm region exhibits broad features of O I, C I, and Mg II in addition to He I λ1.083 μm. We find that both He I λ1.083 μm and λ2.058 μm at +23 days exhibit a "w"-shaped profile, potentially indicative of CSM interaction. The blueshift velocity of the He I λ2.058 μm feature is 10,500 km s$^{-1}$ at −2 days, 10,000 km s$^{-1}$ at +3 days, and 10,500 and 7500 km s$^{-1}$ for the two minima at +23 days for faster and slower components, respectively. In the +23 day spectra, the He I λ1.083 μm feature has the same velocity as the λ2.058 μm features for both components.
(The data used to create this figure are available in the online article.)

The broad optical and NIR helium in the pre- and near-peak spectra (before the appearance of narrow H absorption) indicates that the bulk of the helium is present in the ejecta and therefore that the progenitor star retained a helium layer prior to explosion. On the other hand, the clear postpeak bimodal velocity structure of He I λ2.058 μm, with an emerging component at the same velocity as H and at the same phase, indicates that helium is also present in the CSM. The optical helium features persist until our last spectrum at +160 days, indicating that the CSM interaction-based excitation continues to this late phase.

The [O II] 7320, 7330 Å feature is rare and observed in some SLSNe-I only in the nebular phase when the ejecta is nearly transparent, revealing the inner regions (M. Nicholl et al. 2019). Moreover, the [O III] 4959, 5007 Å feature is seldom seen and requires an excitation mechanism to produce a higher ionization state and a low-density region in the ejecta. In SN 2024afav, the early appearance of [O III] starting at about +50 days and [O II] at +110 days requires such a region in the outer part of the ejecta, as the rest of the spectrum suggests that the ejecta has not reached a nebular state. Such a low-density and high-ionization region in the outer ejecta can be produced by the interaction of ejecta with the CSM, explaining these features at such early epochs (A. Aamer et al. 2024).

Finally, we note that in addition to the emergence of the various interaction-dominated spectral features at about +20 days, the light curve begins to exhibit its first bump and the photospheric temperature exhibits an increase at the same phase—indicators of the same CSM interaction.

Combining the available spectroscopic and photometric information, we can provide a rough picture of the CSM. The multiple bumps (and lack of H emission) point to a patchy or shell-like CSM rather than a smooth wind-like CSM. The CSM is hydrogen- and helium-rich. Using the fastest velocity of 12,000 km s$^{-1}$ for H at +20 days and an explosion date at −49 days (J. R. Farah et al. 2025), we estimate that the nearest CSM shell is located at $\gtrsim 1 \times 10^{15}$ cm; for a CSM velocity of 1000 km s$^{-1}$, this shell would have been ejected 2.2 yr before explosion. The CSM shell is swept by the ejecta, producing a forward shock (N. Smith 2017) that accelerates the CSM to the ejecta velocity, thereby creating the blueshifted narrow H absorption (and high-velocity component of He I) as the shocked region is viewed above the photosphere. This layer encounters no obstacles in the absence of a diffuse CSM until another shell is encountered, at which point it maintains the same velocity (and produces additional bumps in the light curve). The reverse shock produced during the CSM interaction ionizes the outer layers of the ejecta, which are primarily composed of oxygen and helium. This helps to sustain the excitation of helium; moreover, low-density regions in these layers produce the [O III] emission. Subsequently, as the ejecta expand, the low-density regions transition to a lower ionization state, explaining the emergence of [O II] at a later phase than [O III].

To summarize, postpeak CSM interaction provides a consistent explanation for the unusual spectral features and light-curve bumps and their temporal correlation. The interaction-induced forward shock explains the presence of narrow H (and He I), while the reverse shock provides a source of helium excitation and oxygen ionization in the outer ejecta.

### 5.2. Comparison to Previous Multipeaked SLSNe-I

Inspired by the spectral similarity of SN 2024afav to PTF 10hgi and SN 2017egm, we searched for similar events in the SLSN-I sample (S. Gomez et al. 2024; A. Aamer et al. 2025) that satisfy the following criteria: (i) the optical light curve exhibits more than two bumps, and (ii) the spectral coverage extends to $\gtrsim$+100 days. We find four SLSNe—SN 2017egm, SN 2017gci, SN 2019hge, and LSQ14an—that satisfy these criteria. We also include PTF 10hgi in the comparison sample, despite its limited photometric coverage (until phases of $<$ +100 days) and the absence of significant bumps in its light

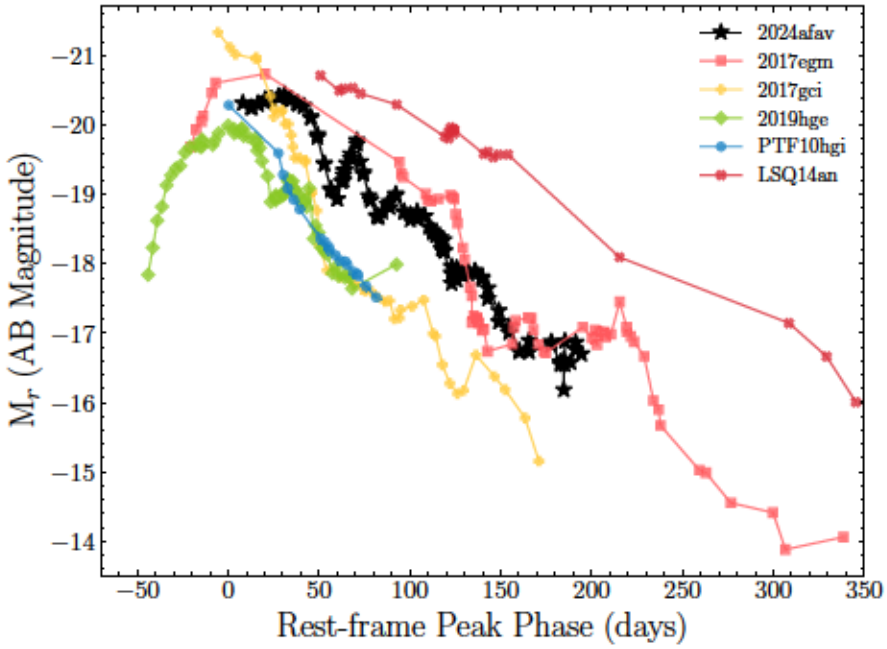


**Figure 7.** The *r*-band light curves of a few SLSNe-I with multiple light-curve bumps. All events except PTF 10hgi have both photometric and spectral coverage well past +100 days, enabling a meaningful comparison. We find that these objects exhibit similar spectral features (see Figure 8), yet they have dissimilar bump shapes.

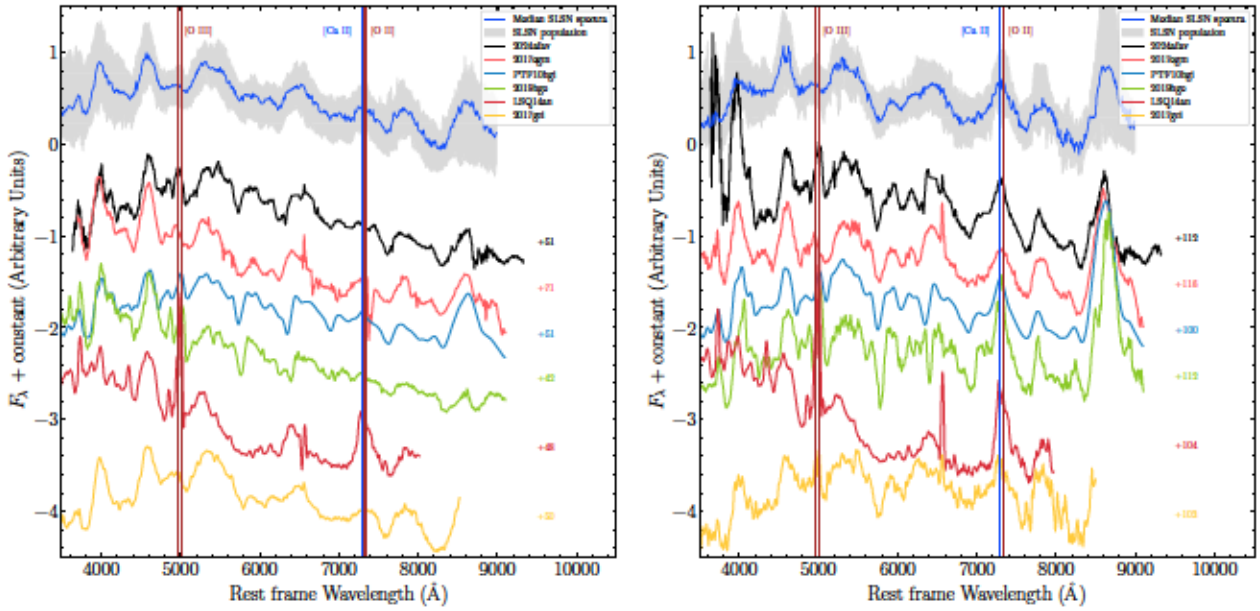


**Figure 8.** Comparison of SN 2024afav spectra at +50 days (left) and +112 days with the SLSN-I population from A. Aamer et al. (2025a) and SLSNe-I with multiple bumps and spectral coverage at similar epochs. These objects represent a small sample of SLSNe-I with multiple bumps in their light curves and a strong presence of the 7300 Å feature. We observe that PTF 10hgi, SN 2019hge, and SN 2024afav show the presence of [O III], He I features at all epochs, and 7300 Å emission features at the +112 day phase. The spectral similarity and bumpy light curves of these objects imply a common progenitor. The other two objects in the spectra exhibit bumpy light curves and 7300 Å emission features, indicating CSM interaction and a potential connection between bumps and CSM interaction in SLSNe-I. Both SN 2017egm and SN 2017gci do not show a strong presence of [O III] features; however, they show [O II] features at late times, implying weaker ionization in ejecta compared to other objects in the sample.

curve, as it exhibits close spectral similarity to SN 2024afav. We caution that this sample is by no means comprehensive, as the identification is limited to visual inspection with the goal of finding similar events, rather than creating a complete sample. The *r*-band light curves of SN 2024afav and the five comparison events are shown in Figure 7.

We compare the spectra of SN 2024afav with the five comparison events at +50 and +110 days in Figure 8. The median SLSN-I spectrum at these phases from A. Aamer et al. (2025a) is shown for reference. The comparison reveals that three of the five events (SN 2017egm, SN 2019hge, and PTF 10hgi) exhibit similar spectral features and evolutionary patterns to SN 2024afav. These events show a remarkably different 5000 Å region compared to median SLSN-I spectra due to the presence of [O III] features. In the +110 day spectra, these four events exhibit a very weak [O I] line and a

stronger 7300 Å feature centered at [O II]. Another noticeable aspect is the presence of strong absorption at the locations of the He I lines. In SN 2024afav (and possibly SN 2019hge; L. Yan et al. 2020), the presence of helium is demonstrated with NIR spectra. In SN 2017egm and PTF 10hgi, previous claims of helium have relied on the optical spectra (L. Yan et al. 2020; J. Zhu et al. 2023); the similarity to SN 2024afav confirms these claims. We conclude that the spectral and light-curve similarities of these four events suggest that they share a similar progenitor configuration.

The other two events in the comparison sample, LSQ 14an and SN 2017gci, exhibit different spectral properties. LSQ 14an exhibits an early presence of the 7300 Å feature (+48 days), which appears asymmetric and centered on the [Ca II] lines and shows no signs of helium features. However, LSQ 14an shows a P Cygni feature at 6300–6400 Å, similar to SN 2024afav, SN 2019hge, and PTF 10hgi, and exhibits strong [O III]. The presence of strong [O III] and 7300 Å features but lack of helium in LSQ 14an indicates that its progenitor may have been completely stripped of its helium layer, and potentially some of its oxygen layer, contributing to the CSM. SN 2017gci has a much weaker 7300 Å feature, centered on the [Ca II] lines, He I features, and no unusual feature in the 6300–6400 Å region. The differences in spectral features between SN 2024afav and LSQ 14an and SN 2017gci suggests that the light-curve bumps do not necessarily require hydrogen or helium in the CSM.

## 6. Conclusions

We presented detailed optical/NIR spectroscopic observations of SN 2024afav, spanning −14 to +160 days, covering the main peak and multiple postpeak light-curve bumps. The key findings are as follows.

1. SN 2024afav has an unusual light curve compared to the majority of SLSNe-I, exhibiting seven significant bumps in the postpeak phase.
2. The prepeak spectra exhibit typical SLSN-I features and closely match the early spectra of SN 2017egm and PTF 10hgi.
3. Postpeak, the spectra show several unusual features indicating CSM interaction with narrow hydrogen and helium shells.
   a. A narrow, high-velocity H absorption feature starting at +20 days.
   b. Persistent optical and NIR He I lines at all available phases. At +23 days, the NIR spectrum showed a high-velocity component of helium at a similar velocity to that of hydrogen, suggesting the presence of helium in both the ejecta and the CSM.
   c. Early appearance of [O III] emission starting at +50 days. Additionally, a strong [O II] + [Ca II] 7300 Å complex starting at +110 days.

   These spectroscopic features indicate that SN 2024afav underwent CSM interaction with narrow shells that primarily consist of hydrogen, with a possibly small amount of helium.
4. We compare SN 2024afav with a subset of SLSNe-I that exhibit bumpy light curves with late-time spectral coverage. These objects exhibit some combination of the early presence of [O III], an excess of the [O II] + [Ca II] complex, and persistent helium features until late phases, suggestive of CSM interaction. Our comparison sample suggests that the bumps in the light curves and these unusual features are potentially correlated.

In the upcoming era of the Rubin Observatory/LSST, detailed late-time light curves of SLSNe-I will be available in abundance. Systematic follow-up of events with multiple bumps will elucidate the fraction of events in which CSM interaction can significantly modify the postpeak light curves and spectra.

## Acknowledgments

We thank Kali Salmas, Alejandra Milone, and Benjamin Weiner for scheduling the MMT Binospec observations and Yuri Beletsky for performing the Magellan LDSS-3 observations.

The Berger Time-Domain research group at Harvard is supported by the NSF and NASA grants. The LCO supernova group is supported by NSF grants AST-1911151 and AST-1911225. This work is supported by the National Science Foundation under Cooperative Agreement PHY-2019786 (The NSF AI Institute for Artificial Intelligence and Fundamental Interactions, http://iaifi.org/).

K.A.B. is supported by an LSST-DA Catalyst Fellowship; this publication was thus made possible through the support of grant 62192 from the John Templeton Foundation to LSST-DA.

This Letter includes data gathered with the 6.5 m Magellan Telescopes located at Las Campanas Observatory, Chile. The LCO team is supported by NSF grants AST-2308113 and AST-1911151.

Observations reported here were obtained at the MMT Observatory, a joint facility of the Smithsonian Institution and the University of Arizona. This Letter uses data products produced by the OIR Telescope Data Center, supported by the Smithsonian Astrophysical Observatory.

This work makes use of observations from the Las Cumbres Observatory global telescope network. The authors wish to recognize and acknowledge the very significant cultural role and reverence that the summit of Haleakalā has always had within the indigenous Hawaiian community. We are most fortunate to have the opportunity to conduct observations from the mountain.

We acknowledge the use of public data from the Swift data archive.

This research made use of `PypeIt`,[15] a `python` package for semiautomated reduction of astronomical slit-based spectroscopy (J. X. Prochaska et al. 2020a, 2020b). This research made use of WISeREP[16] (O. Yaron & A. Gal-Yam 2012).

This work has made use of data from the Zwicky Transient Facility (ZTF). ZTF is supported by NSF grant No. AST-1440341 and a collaboration including Caltech, IPAC, the Weizmann Institute for Science, the Oskar Klein Center at Stockholm University, the University of Maryland, the University of Washington, Deutsches Elektronen-Synchrotron and Humboldt University, Los Alamos National Laboratories, the TANGO Consortium of Taiwan, the University of

[15] https://pypeit.readthedocs.io/en/latest/
[16] https://wiserep.org

Wisconsin–Milwaukee, and Lawrence Berkeley National Laboratories. Operations are conducted by COO, IPAC, and UW. The ZTF forced-photometry service was funded under the Heising-Simons Foundation grant No. 12540303 (PI: Graham).

This work has made use of data from the Asteroid Terrestrial-impact Last Alert System (ATLAS) project. The Asteroid Terrestrial-impact Last Alert System (ATLAS) project is primarily funded to search for near-Earth asteroids through NASA grants NN12AR55G, 80NSSC18K0284, and 80NSSC18K1575; by-products of the NEO search include images and catalogs from the survey area. This work was partially funded by Kepler/K2 grant J1944/80NSSC19K0112 and HST GO-15889 and STFC grants ST/T000198/1 and ST/S006109/1. The ATLAS science products have been made possible through the contributions of the University of Hawaii Institute for Astronomy, the Queen's University Belfast, the Space Telescope Science Institute, the South African Astronomical Observatory, and the Millennium Institute of Astrophysics (MAS), Chile.

This research has made use of the NASA Astrophysics Data System (ADS), the NASA/IPAC Extragalactic Database (NED), and the NASA/IPAC Infrared Science Archive (IRSA, which is funded by NASA and operated by the California Institute of Technology) and IRAF (which is distributed by the National Optical Astronomy Observatory, NOAO, operated by the Association of Universities for Research in Astronomy, AURA, Inc., under cooperative agreement with the NSF).

TNS is supported by funding from the Weizmann Institute of Science, as well as grants from the Israeli Institute for Advanced Studies and the European Union via ERC grant No. 725161.

*Facilities:* ATLAS, FLWO 1.2m, LCO, Magellan:Clay (Magellan II Landon Clay Telescope), MMT (MMT at Fred Lawrence Whipple Observatory), Swift (UVOT and XRT), and PO:1.2m (Palomar Observatory's 1.2 meter Samuel Oschin Telescope).

*Software:* astropy (Astropy Collaboration et al. 2013, 2018; Astropy Collaboration et al. 2022), `SExtractor` (E. Bertin & S. Arnouts 1996), `NumPy` (C. R. Harris et al. 2020), `photutils` (L. Bradley et al. 2022), `PyRAF` (Science Software Branch at STScI 2012), `SciPy` (P. Virtanen et al. 2020), `UVOTSOURCE`, `extrabol` (I. Thornton et al. 2024), `PypeIt` (J. X. Prochaska et al. 2020a), `lcogtsnpipe` (S. Valenti et al. 2016), and `MOSFiT` (J. Guillochon et al. 2017).

## Appendix
## Data Tables

This section contains additional data used in the Figures. Table 2 contains all photometry used in Figure 1. Table 3 contains velocity evolution measurements using features of Si II 6355 Å, O, I, 6158 Å, and O I 7774 Å features at all spectroscopic epochs. Table 4 lists $L_{7300}/L_{6300}$ estimated using [O I], [O II], and [O III] features.

**Table 2**
Photometry of SN 2024afav

| MJD | Filter | Magnitude α e_magnitude | Telescope |
|---|---|---|---|
| 60665.33 | *o* | 18.53 α 0.09 | ATLAS |
| 60666.34 | *o* | 18.57 α 0.09 | ATLAS |
| 60672.65 | *o* | 18.03 α 0.05 | ATLAS |
| 60674.33 | *o* | 17.92 α 0.04 | ATLAS |
| 60676.06 | *c* | 17.70 α 0.03 | ATLAS |
| 60677.31 | *o* | 17.85 α 0.04 | ATLAS |
| 60678.31 | *o* | 17.71 α 0.03 | ATLAS |
| 60679.05 | *c* | 17.56 α 0.02 | ATLAS |
| 60680.04 | *c* | 17.54 α 0.03 | ATLAS |
| 60681.32 | *o* | 17.55 α 0.03 | ATLAS |

**Notes.** All magnitudes are in the AB system and corrected for Galactic extinction.

(This table is available in its entirety in machine-readable form in the online article.)

**Table 3**
Velocity Evolution Measurement Using the Spectral Sequence of SN 2024afav. The entries marked have a poor profile fit and therefore are less reliable.

| Phase (days) | Velocity (km s$^{-1}$) | | |
|---|---|---|---|
| | Si II 6355 Å | O I 6158 Å | O I 7774 Å |
| −14 | 11,707 ± 483 | ... | 6729 ± 242* |
| −4 | 8911 ± 395 | 6540 ± 54* | 7037 ± 543 |
| +20 | 7858 ± 41 | 8116 ± 972 | 7190 ± 141 |
| +24 | 7388 ± 39 | 7473 ± 49 | 6800 ± 43 |
| +27 | 7417 ± 33 | 7387 ± 46 | 7304 ± 133 |
| +30 | 7171 ± 25 | 6418 ± 95 | 6683 ± 74 |
| +47 | 6282 ± 64 | 6411 ± 126 | 6535 ± 68 |
| +51 | 5443 ± 43 | 6415 ± 66 | 6341 ± 108 |
| +53 | ... | 5976 ± 76* | 6426 ± 37 |
| +54 | 5439 ± 83 | 6392 ± 105 | 5971 ± 71 |
| +63 | 4799 ± 75 | 6663 ± 231 | 5685 ± 211 |
| +74 | 4786 ± 84 | 6284 ± 778* | 4254 ± 1010* |
| +91 | 4131 ± 566 | 6355 ± 444 | 5906 ± 127 |
| +112 | 3657 ± 57 | 4879 ± 162 | 5434 ± 222 |
| +139 | ... | 5851 ± 140* | 5008 ± 51 |
| +160 | 6140 ± 432* | 5224 ± 104 | 6603 ± 3289* |

**Table 4**
Area *in* Unit of Flux Density for the [O III], [O II], and [O I] Features, Estimated Using Line Profile Fitting

| Phase (days) | Area | | | | | $L_{7300}/L_{6300}$ |
|---|---|---|---|---|---|---|
| | [O III] 4959 Å | [O III] 5007 Å | [O I] 6300 Å | [O II] 7319, 7330 Å | [Ca II] 7291, 7324 Å | |
| +112 | 9.29 ± 2.25 | 48.51 ± 3.86 | 5.32 ± 0.57 | 14.26 ± 3.94 | 11.40 ± 4.21 | 4.82 ± 1.14 |
| +139 | 10.81 ± 1.95 | 44.31 ± 3.16 | 3.12 ± 0.15 | 65.66 ± 5.92 | 43.50 ± 4.87 | 34.99 ± 2.50 |
| +160 | 4.70 ± 0.92 | 34.72 ± 1.53 | 6.07 ± 5.18 | 120.49 ± 5.40 | 206.05 ± 15.49 | 53.80 ± 46.24 |

**Note.** We estimated the $L_{7300}/L_{6300}$ ratio for each epoch and found an increasing ratio trend.

## ORCID iDs

Harsh Kumar https://orcid.org/0000-0003-0871-4641
Peter K. Blanchard https://orcid.org/0000-0003-0526-2248
Edo Berger https://orcid.org/0000-0002-9392-9681
Wasundara Athukoralalage https://orcid.org/0000-0002-2866-6416
Daichi Hiramatsu https://orcid.org/0000-0002-1125-9187
Sebastian Gomez https://orcid.org/0000-0001-6395-6702
Moira Andrews https://orcid.org/0000-0002-1895-6639
K. Azalee Bostroem https://orcid.org/0000-0002-4924-444X
Joseph R. Farah https://orcid.org/0000-0003-4914-5625
D. Andrew Howell https://orcid.org/0000-0003-4253-656X
Curtis McCully https://orcid.org/0000-0001-5807-7893

## References

Aamer, A., Nicholl, M., Gomez, S., et al. 2025, MNRAS, 541, 2674
Aamer, A., Nicholl, M., Jerkstrand, A., et al. 2024, MNRAS, 527, 11970
Angus, C. R., Smith, M., Sullivan, M., et al. 2019, MNRAS, 487, 2215
Astropy Collaboration, Price-Whelan, A. M., Lim, P. L., et al. 2022, ApJ, 935, 167
Astropy Collaboration, Price-Whelan, A. M., Sipőcz, B. M., et al. 2018, AJ, 156, 123
Astropy Collaboration, Robitaille, T. P., Tollerud, E. J., et al. 2013, A&A, 558, A33
Bertin, E., & Arnouts, S. 1996, A&AS, 117, 393
Blanchard, P. K., Berger, E., Gomez, S., et al. 2025, arXiv:2511.10747
Bose, S., Dong, S., Pastorello, A., et al. 2018, ApJ, 853, 57
Bradley, L., Sipőcz, B., Robitaille, T., et al. 2022, astropy/photutils: v1.5.0, Zenodo, doi:10.5281/zenodo.6825092
Brown, T. M., Baliber, N., Bianco, F. B., et al. 2013, PASP, 125, 1031
Chen, T.-W., Smartt, S. J., Yates, R. M., et al. 2017, MNRAS, 470, 3566
Chen, Z. H., Yan, L., Kangas, T., et al. 2023, ApJ, 943, 41
Chevalier, R. A., & Fransson, C. 2017, in Handbook of Supernovae, ed. A. W. Alsabti & P. Murdin (Springer Cham), 875, doi: 10.1007/978-3-319-21846-5_34
Chomiuk, L., Chornock, R., Soderberg, A. M., et al. 2011, ApJ, 743, 114
Dessart, L. 2024a, A&A, 692, A204
Dessart, L. 2024b, arXiv:2405.04259
Dessart, L., & Hillier, D. J. 2022, A&A, 660, L9
Dessart, L., Hillier, D. J., Audit, E., Livne, E., & Waldman, R. 2016, MNRAS, 458, 2094
de Wet, S., Wichern, H., Leloudas, G., & Yaron, O. 2025, TNSCR, 337, 1
Dexter, J., & Kasen, D. 2013, ApJ, 772, 30
Eikenberry, S., Elston, R., Raines, S. N., et al. 2006, SPIE, 6269, 626917
Elias, J. H., Joyce, R. R., Liang, M., et al. 2006, SPIE, 6269, 62694C
Evans, P. A., Beardmore, A. P., Page, K. L., et al. 2007, A&A, 469, 379
Evans, P. A., Beardmore, A. P., Page, K. L., et al. 2009, MNRAS, 397, 1177
Fabricant, D., Fata, R., Epps, H., et al. 2019, PASP, 131, 075004
Farah, J. R., Prust, L. J., Howell, D. A., et al. 2025, arXiv:2509.08051
Filippenko, A. V. 1982, PASP, 94, 715
Fiore, A., Chen, T. W., Jerkstrand, A., et al. 2021, MNRAS, 502, 2120
Fitzpatrick, E. L. 1999, PASP, 111, 63
Gal-Yam, A. 2012, Sci, 337, 927
Gal-Yam, A. 2019a, ApJ, 882, 102
Gal-Yam, A. 2019b, ARA&A, 57, 305
Gal-Yam, A., Mazzali, P., Ofek, E. O., et al. 2009, Natur, 462, 624
Gomez, S., Nicholl, M., Berger, E., et al. 2024, MNRAS, 535, 471
Guillochon, J., Nicholl, M., Villar, V. A., et al., 2017 MOSFiT: Modular Open-Source Fitter for Transients, Astrophysics Source Code Library, ascl:1710.006
Harris, C. R., Millman, K. J., van der Walt, S. J., et al. 2020, Natur, 585, 357

Hogg, D. W., Baldry, I. K., Blanton, M. R., & Eisenstein, D. J. 2002, arXiv: astro-ph/0210394
Hosseinzadeh, G., Berger, E., Metzger, B. D., et al. 2022, ApJ, 933, 14
Howell, D. A. 2017, in Handbook of Supernovae, ed. A. W. Alsabti & P. Murdin, 431, 10.1007/978-3-319-21846-5_41
Hsu, B., Blanchard, P. K., Berger, E., & Gomez, S. 2024, ApJ, 961, 169
Hsu, B., Hosseinzadeh, G., & Berger, E. 2021, ApJ, 921, 180
Inserra, C., Nicholl, M., Chen, T. W., et al. 2017, MNRAS, 468, 4642
Kasen, D., & Bildsten, L. 2010, ApJ, 717, 245
Kelson, D. D. 2003, PASP, 115, 688
Kelson, D. D., Illingworth, G. D., van Dokkum, P. G., & Franx, M. 2000, ApJ, 531, 159
Kozyreva, A., & Blinnikov, S. 2015, MNRAS, 454, 4357
Kumar, A., Ramsay, G., Ackley, K., et al. 2024, TNSTR, 5091, 1
Kumar, H., Berger, E., Blanchard, P. K., et al. 2025, ApJ, 987, 127
Lin, W., Wang, X., Yan, L., et al. 2023, NatAs, 7, 779
Lunnan, R., Chornock, R., Berger, E., et al. 2014, ApJ, 787, 138
Lunnan, R., Chornock, R., Berger, E., et al. 2018a, ApJ, 852, 81
Lunnan, R., Fransson, C., Vreeswijk, P. M., et al. 2018b, NatAs, 2, 887
Margutti, R., Chornock, R., Metzger, B. D., et al. 2018, ApJ, 864, 45
Mazzali, P. A., Sullivan, M., Pian, E., Greiner, J., & Kann, D. A. 2016, MNRAS, 458, 3455
Metzger, B. D., Margalit, B., Kasen, D., & Quataert, E. 2015, MNRAS, 454, 3311
Montero-Dorta, A. D., & Prada, F. 2009, MNRAS, 399, 1106
Moriya, T. J. 2024, arXiv:2407.12302
Moriya, T. J., Nicholl, M., & Guillochon, J. 2018, ApJ, 867, 113
Nicholl, M. 2021, A&G, 62, 5.34
Nicholl, M., Berger, E., Blanchard, P. K., Gomez, S., & Chornock, R. 2019, ApJ, 871, 102
Nicholl, M., Berger, E., Smartt, S. J., et al. 2016, ApJ, 826, 39
Nicholl, M., Blanchard, P. K., Berger, E., et al. 2018, ApJL, 866, L24
Nicholl, M., Guillochon, J., & Berger, E. 2017, ApJ, 850, 55
Nicholl, M., Smartt, S. J., Jerkstrand, A., et al. 2015, MNRAS, 452, 3869
Perley, D. A., Quimby, R. M., Yan, L., et al. 2016, ApJ, 830, 13
Prentice, S. J., Inserra, C., Schulze, S., et al. 2021, MNRAS, 508, 4342
Prochaska, J. X., Hennawi, J., Cooke, R., et al. 2020b, pypeit/PypeIt: Release v1.0.0, Zenodo, doi:10.5281/zenodo.3743493
Prochaska, J. X., Hennawi, J. F., Westfall, K. B., et al. 2020a, JOSS, 5, 2308
Pursiainen, M., Leloudas, G., Paraskeva, E., et al. 2022, A&A, 666, A30
Quimby, R. M., De Cia, A., Gal-Yam, A., et al. 2018, ApJ, 855, 2
Quimby, R. M., Kulkarni, S. R., Kasliwal, M. M., et al. 2011, Natur, 474, 487
Schlafly, E. F., & Finkbeiner, D. P. 2011, ApJ, 737, 103
Schulze, S., Fransson, C., Kozyreva, A., et al. 2024, A&A, 683, A223
Science Software Branch at STScI, 2012 PyRAF: Python Alternative for IRAF, Astrophysics Source Code Library, ascl:1207.011
Selver, M. A., Secmen, M., & Zoral, E. Y. 2018, JPhCS, 1141, 012151
Shahbandeh, M., Hsiao, E. Y., Ashall, C., et al. 2022, ApJ, 925, 175
Smith, N. 2017, in Handbook of Supernovae, ed. A. W. Alsabti & P. Murdin, 403, doi: 10.1007/978-3-319-21846-5_38
Sorokina, E., Blinnikov, S., Nomoto, K., Quimby, R., & Tolstov, A. 2016, ApJ, 829, 17
Stevenson, K. B., Bean, J. L., Seifahrt, A., et al. 2016, ApJ, 817, 141
Thornton, I., Villar, V. A., Gomez, S., & Hosseinzadeh, G. 2024, RNAAS, 8, 48
Tolstov, A., Nomoto, K., Blinnikov, S., et al. 2017, ApJ, 835, 266
Tonry, J. L., Denneau, L., Heinze, A. N., et al. 2018, PASP, 130, 064505
Valenti, S., Howell, D. A., Stritzinger, M. D., et al. 2016, MNRAS, 459, 3939
Valenti, S., Sand, D., Pastorello, A., et al. 2014, MNRAS, 438, L101
Virtanen, P., Gommers, R., Oliphant, T. E., et al. 2020, NatMe, 17, 261
Wheeler, J. C., Chatzopoulos, E., Vinkó, J., & Tuminello, R. 2017, ApJL, 851, L14
Willingale, R., Starling, R. L. C., Beardmore, A. P., Tanvir, N. R., & O'Brien, P. T. 2013, MNRAS, 431, 394
Woosley, S. E. 2010, ApJL, 719, L204
Yan, L., Lunnan, R., Perley, D. A., et al. 2017, ApJ, 848, 6
Yan, L., Perley, D. A., Schulze, S., et al. 2020, ApJL, 902, L8
Yan, L., Quimby, R., Ofek, E., et al. 2015, ApJ, 814, 108
Yaron, O., & Gal-Yam, A. 2012, PASP, 124, 668
Zhang, B., Li, L., Dai, Z.-G., & Zhong, S.-Q. 2025, ApJ, 985, 172
Zhu, J., Jiang, N., Dong, S., et al. 2023, ApJ, 949, 23
Zhu, J.-P., Liu, L.-D., Yu, Y.-W., et al. 2024, ApJL, 970, L42